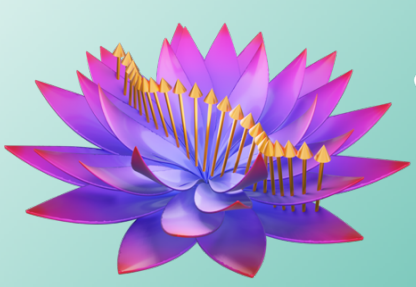

NIMFEIA

Deliverable D2.1

Report on the characterisation of vortex-based magnon reservoirs

Project Number	101070290
Project name	Nonlinear Magnons for Reservoir Computing in Reciprocal Space
Project acronym	NIMFEIA
Work Package	WP2 Laboratory-scale experiments
Type	Report
Dissemination level	Public
Lead Beneficiary	HZDR
Due date of delivery	Month 12 – September 2023
Author(s)	Katrin Schultheiss (HZDR), Lukas Körber (HZDR), Christopher Heins (HZDR), Helmut Schultheiss (HZDR), Attila Kákay (HZDR), Joo-Von Kim (UPS), Sonia Thlang (UPS)

Disclaimer:

The NIMFEIA project has received funding by the European Union's Research and Innovation Programme Horizon Europe under grant agreement No 101070290. However, views and opinions expressed in this document are those of the authors only and do not necessarily reflect those of the European Union. The European Union cannot be held responsible for them.

Table of contents

1. Introduction

A key challenge in modern electronics is to develop low-power solutions for information processing tasks such as pattern recognition on noisy or incomplete data. One promising approach is physical reservoir computing, which exploits the nonlinearity and recurrence of dynamical systems (the reservoir) as a computational resource[1,2,3,4]. Examples include a diverse range of materials such as water[5], optoelectronic systems[6,7,8,9], silicon photonics[10], microcavity lasers[11], organic electrochemical transistors[12], dynamic memristors[13], nanowire networks[14], and magnetic devices[15,16,17,18,19,20,21]. The physical reservoir embodies a recurrent neural network. A natural implementation comprises interconnected nonlinear elements in space (spatial multiplexing, Fig. 1a), where information is fed into the system via input nodes representing distinct spatial elements, and the dynamical state is read out through another set of output nodes. Another approach involves mapping the network onto a set of virtual nodes in time by using delayed-feedback dynamics on a single nonlinear node (temporal multiplexing, Fig. 1b), which reduces the complexity in spatial connectivity at the expense of more intricate time-dependent signal processing.

In the NIMFEIA project, we study an alternative paradigm by exploiting the dynamics in the modal space of a magnetic element. This scheme relies on magnon interactions in magnetic materials whereby inputs and outputs correspond to particular eigenmodes of a micromagnetic state. Micrometer-sized magnetic structures can exhibit hundreds of eigenmodes with frequencies in the GHz range[22]. Processes such as three magnon-scattering interconnect these modes with each other and, with that, provide the nonlinearity and recurrence required for computing. We refer to this approach as modal multiplexing with signals evolving in reciprocal space, in which the actual computa-

---

[1] Jaeger, H. The"echo state" approach to analysing and training recurrent neural networks-with an erratum note. *Bonn, Germany: German National Research Center for Information Technology GMD Technical Report* 148, 13(2001).

[2] Nakajima, K. Physical reservoir computing–an introductory perspective. *Jpn. J. Appl. Phys.* 59, 060,501 (2020).

[3] Tanaka, G. et al. Recent advances in physical reservoir computing: a review. *Neural Netw.* 115,100–123 (2019).

[4] Maass, W., Natschlger, T. & Markram, H. Real-time computing without stable states: a new framework for neural computation based on perturbations. *Neural Comput.* 14, 2531–2560 (2002).

[5] Fernando, C., Sojakka, S. Pattern Recognition in a Bucket. pp. 588–597 https://doi.org/10.1007/978-3-540-39432-7_63 (2003).

[6] Appeltant, L. et al. Information processing using a single dynamical node as complex system. *Nat. Commun.* 2, 468 (2011).

[7] Paquot, Y. et al. Optoelectronic reservoir computing. *Sci. Rep.* 2, 287 (2012).

[8] Ortín, S. et al. A unified framework for reservoir computing and extreme learning machines based on a single time-delayed neuron. *Sci. Rep.* 5, 14, 945 (2015).

[9] Larger, L. et al. High-speed photonic reservoir computing using a time-delay-based architecture: million words per second classification. *Phys. Rev. X* 7, 011,015 (2017).

[10] Vandoorne, K. et al. Experimental demonstration of reservoir computing on a silicon photonics chip. *Nat. Commun.* 5, 1–6(2014).

[11] Sunada, S. & Uchida, A. Photonic reservoir computing based on nonlinear wave dynamics at microscale. *Sci. Rep.* 9, 19, 078 (2019).

[12] Cucchi, M. et al. Reservoir computing with biocompatible organic electrochemical networks for brain-inspired biosignal classification. *Sci. Adv.* 7, eabh0693 (2021).

[13] Zhong, Y. et al. Dynamic memristor-based reservoir computing for high-efficiency temporal signal processing. *Nat. Commun.* 12, 408 (2021).

[14] Milano, G. et al. In materia reservoir computing with a fully memristive architecture based on self-organizing nanowire networks. *Nat. Mater.* 21, 195–202 (2022).

[15] Torrejon, J. et al. Neuromorphic computing with nanoscale spintronic oscillators. *Nature* 547, 428–431 (2017).

[16] Nakane, R., Tanaka, G. & Hirose, A. Reservoir computing with spin waves excited in a garnet film. *IEEE Access* 6, 4462–4469 (2018).

[17] Kanao, T. et al. Reservoir computing on spin-torque oscillator array. *Phys. Rev. Appl.* 12, 024, 052(2019).

[18] Watt, S., Kostylev, M., Ustinov, A. B. & Kalinikos, B. A. Implementing a magnonic reservoir computer model based on time-delay multiplexing. *Phys. Rev. Appl.* 15, 064, 060 (2021).

[19] Nakane, R., Hirose, A. & Tanaka, G. Spin waves propagating through a stripe magnetic domain structure and their applications to reservoir computing. *Phys. Rev. Res.* 3, 033,243 (2021).

[20] Gartside, J. C. et al. Reconfigurable training and reservoir computing in an artificial spin-vortex ice via spin-wave fingerprinting. *Nat. Nanotechnol.* 17,460–469 (2022).

[21] Ababei, R. V. et al. Neuromorphic computation with a single magnetic domain wall. *Sci. Rep.* 11,1–13 (2021).

[22] Schultheiss, K. et al. Excitation of whispering gallery magnons in a magnetic vortex. *Phys. Rev. Lett.* 122, 097, 202 (2019).

tion is performed. This is distinct from other wave-based schemes where information is processed with wave propagation and interference in real space and differs from temporal multiplexing where virtual nodes are constructed with delayed feedback. The latter also includes reservoirs based on optical cavities where multimode dynamics (such as frequency combs) are exploited but the output spaces are still constructed by temporal multiplexing.

2. The working principle of a magnon scattering reservoir

As a first proof of concept, we illustrate the concept of modal multiplexing with a pattern recognition task using a magnon-scattering reservoir (MSR). The results of this work have been published in Nature Communications[23]. The patterns comprise a sequence of symbols "A" and "B" represented by radiofrequency (rf) signals, which consist of sine wave pulses with two distinct frequencies, f_A and f_B, and amplitudes $b_{rf,A}$ and $b_{rf,B}$ as shown in Fig. 1d. An example of the power spectrum of the input sequence is given in Fig. 1e. The rf pulses generate oscillating magnetic fields along the z-direction through an Ω-shaped antenna, which surrounds a 5-µm wide and 50-nm thick $Ni_{81}Fe_{19}$ disk

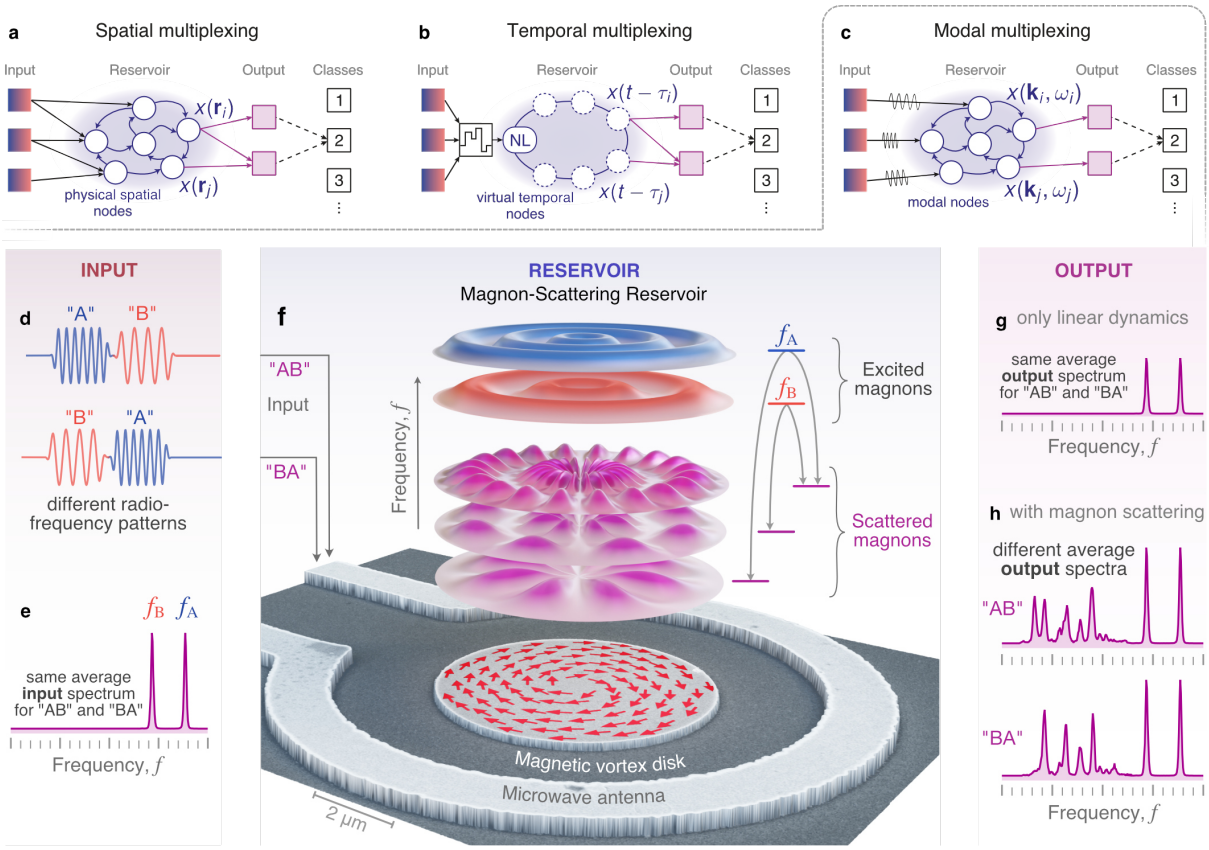

Fig. 1: Working principle of a magnon-scattering reservoir (MSR). Sketches of different reservoirs based on (a) spatial, (b) temporal, and (c) modal multiplexing, the concept behind the MSR. (d) Radiofrequency pulses with different temporal order but (e) the same average frequency content are used to trigger (f) nonlinear scattering between the magnon eigenmodes in a magnetic vortex disk. The dynamic response is experimentally detected using Brillouin-light-scattering microscopy. In contrast to a linear system (g), the MSR produces different outputs depending on the temporal order of the input (h). Taken from [L. Körber et al., *Nature Comm.* 14, 3954 (2023)].

[23] Körber, L. et al. Pattern recognition in reciprocal space with a magnon-scattering reservoir. *Nature Comm.* 14, 3954 (2023).

which hosts a magnetic vortex as a ground state (Fig. 1f). f_A and f_B are chosen to coincide with the frequencies of primary radial eigenmodes of the vortex, which, when excited above a given threshold, result in the excitation of secondary azimuthal eigenmodes through three-magnon splitting processes[24]. In our previous work[25], we have shown that individual three-magnon splitting channels, e.g. exciting only f_A, can be stimulated below their threshold power, and their temporal evolution is significantly modified by additionally exciting one of the secondary modes. This stimulation was achieved by magnons propagating in a waveguide adjacent to the vortex disk. As a logical extension, the role of the stimulating magnon is now provided by the secondary modes of another (active) three-magnon channel f_B, a process that we refer to as cross-stimulated three-magnon splitting. The operation of our magnon-scattering reservoir strongly relies on the fact that the cross-stimulation between f_A and f_B is not reciprocal due to the involved nonlinear transients. In other words, the effect of channel f_A on the channel f_B via cross-stimulation differs from the feedback of f_B on f_A.

The power spectrum of excited magnons is measured experimentally on 10 different positions (indicated in Fig. 2a through time-resolved Brillouin light scattering microscopy (TR-μBLS). For this technique, a monochromatic 532-nm laser (CW) is focused onto the sample surface using a 100x microscope lens with a numerical aperture of 0.7. The backscattered light is then directed into a Tandem Fabry-Pérot interferometer using a beam splitter (BS) to measure the frequency shift caused by the inelastic scattering of photons and magnons. Control signals that encode the current state of the interferometer, signals of the photon counter inside the interferometer, and a clock signal from the pattern generator are acquired continuously by a time-to-digital converter. From these data, the temporal evolution of the magnon spectra with respect to the stroboscopic microwave excitation is reconstructed. During the experiments, the investigated structure is imaged using a red LED and a CCD camera (red beam path in Fig. 2b). Displacements and drifts of the sample are tracked by an

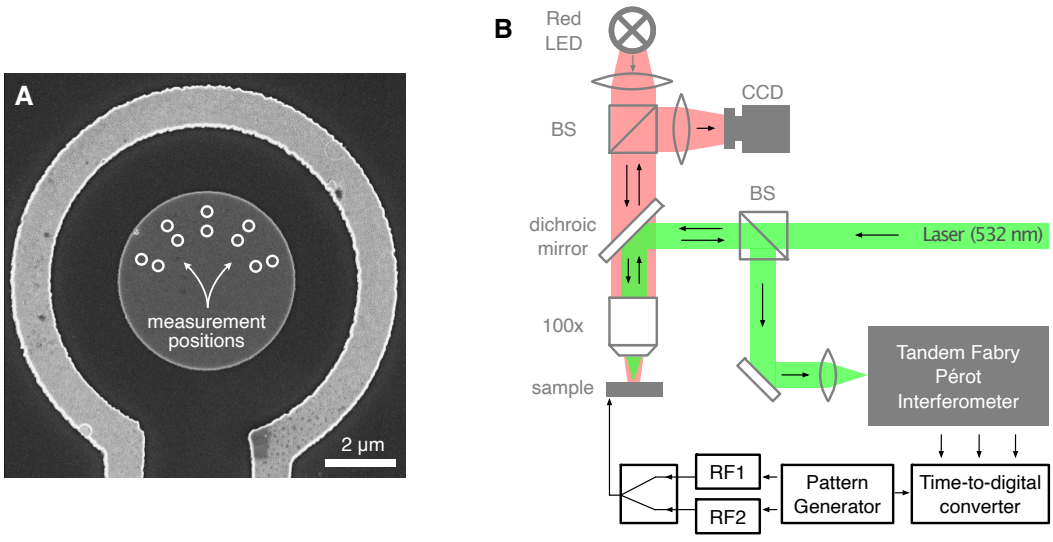

Fig. 2: (a) Scanning-electron-microscopy image of the magnetic disk used as a magnon-scattering reservoir which is surrounded by the Ω-shaped microwave antenna. Hallow circles mark the positions of the microfocused laser spot in the Brillouin-light-scattering-microscopy experiments. (b) Schematics of the experimental setup, including the Brillouin-light-scattering optics and the peripherie for signal generation. Taken from [L. Körber et al., *Nature Comm.* 14, 3954 (2023)].

[24] Schultheiss, K. et al. Excitation of whispering gallery magnons in a magnetic vortex. *Phys. Rev. Lett*. 122, 097, 202 (2019).

[25] Körber, L. et al. Nonlocal stimulation of three-magnon splitting in a magnetic vortex. *Phys. Rev. Lett*. 125, 207, 203 (2020).

image recognition algorithm and compensated by the sample positioning system (XMS linear stages by Newport). The laser and imaging beam path were separated by the dichroic mirror shown in Fig. 2b. To ensure that all stationary magnon modes are measured, the signal is integrated over 10 positions across half the disk (Fig. 2a).

It is important to note that in the linear response regime, neither the input spectrum (Fig. 1e) nor the directly excited magnon spectrum (Fig. 1g) gives any information about the sequence of “A” and “B” (e.g., “AB” and “BA” are equivalent). This means that no linear classifier can be employed. However, when nonlinear processes are at play, magnon scattering, and associated transient processes result in distinct spectral signatures that can be used to distinguish between different input sequences (Fig. 1h).

Figure 3 illustrates the role of three-magnon splitting (3MS), the primary nonlinear process at play in the magnon reservoir, in which a strongly excited primary magnon splits into two secondary magnons under the conservation of energy and momentum. In experiments, we choose 20-ns pulses of f_A = 8.9GHz (20 dBm) and f_B = 7.4 GHz (24 dBm), which excite different radial modes of the

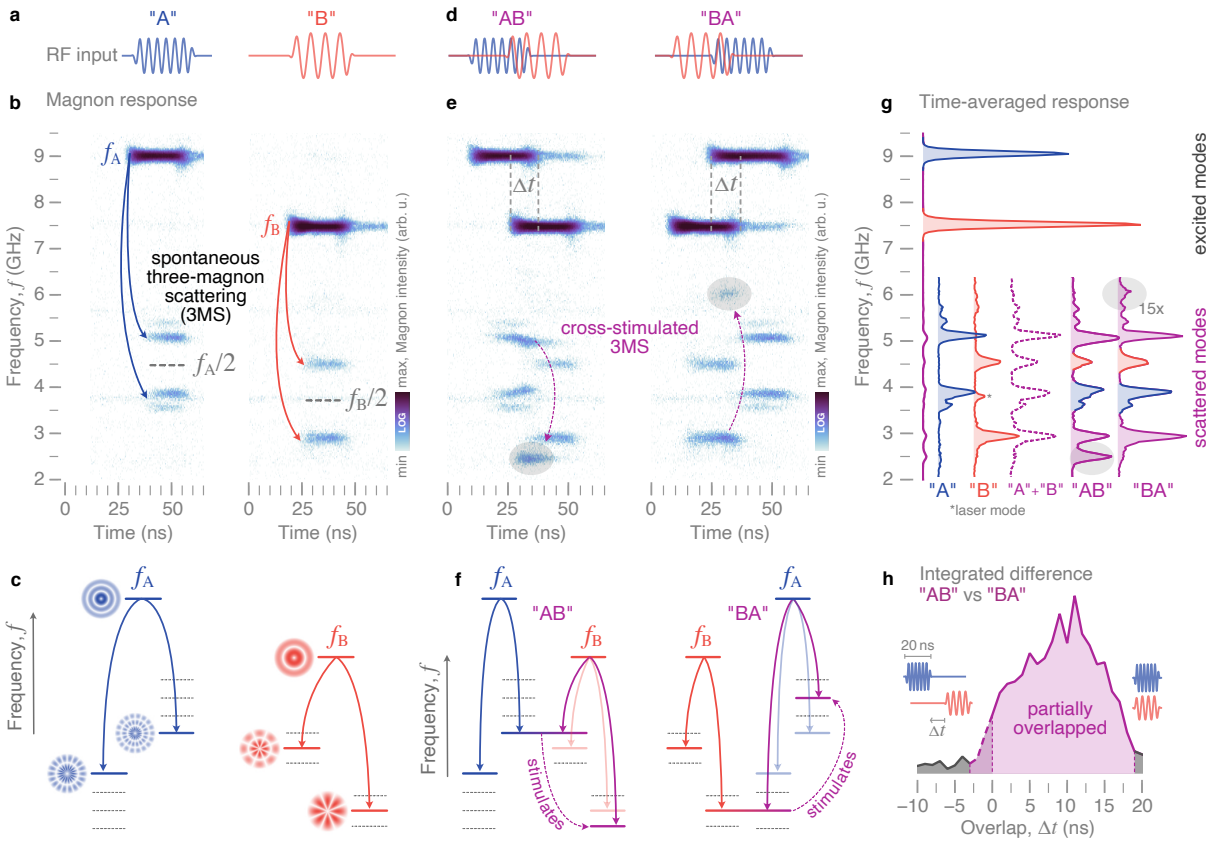

Fig. 3: Physical background of the magnon-scattering reservoir (MSR). When pumped strongly by microwave fields (a), a directly-excited primary magnon splits into two secondary magnons (b) via spontaneous 3MS (c). (b) Time-resolved frequency response of the MSR to two different input frequencies experimentally measured with TR-μBLS. (d) Driving the MSR with two different, temporally overlapping microwave pulses “A” and “B” leads to (e), (f) cross-stimulated 3MS between the channels and to additional peaks in the measured frequency response. (g) Experimentally measured output spectra integrated over time which is different depending on the temporal order of the pulses. Different colors denote different contributions from the two input signals. Blue peaks result from input “A” only, red peaks from “B”, and purple peaks from cross-stimulation. (h) The integrated difference between the spectra of “AB” and “BA” shows that the responses are different when the pulses overlap in time. Taken from [L. Körber et al., *Nature Comm.* 14, 3954 (2023)].

vortex above their respective power threshold for three-magnon splitting, to represent the symbols “A” and “B”, respectively (Fig. 3a). The magnon intensity is probed as a function of frequency and time using TR-µBLS and is colour-coded in Fig. 3b. We measure not only the directly excited primary magnons at f_A and f_B but also magnons at frequencies around half the respective excitation frequencies which result from the nonlinearity of spontaneous three-magnon splitting (see Fig. 3c). Only the scattering channel with the lowest power threshold is active while other allowed scattering channels remain silent (depicted by dotted lines in Fig. 3c).

Cross-stimulation occurs when signals “A” and “B” overlap in time, as shown in Fig. 3d. Two different primary magnons that share a common secondary mode, as is depicted in Fig. 3f, can result in two three-magnon splitting channels that mutually cross-stimulate each other, even below their intrinsic thresholds and along silent channels. Thus, within the overlap interval, the pumped secondary magnon of the first symbol influences the primary mode scattering of the second symbol, and vice versa, leading to the primary mode scattering into multiple pairs of secondary modes (Fig. 3e).

Because cross-stimulation strongly depends on the temporal order of the primary excitation (Fig. 3f), it provides an important physical resource for processing the temporal sequence of our input signals. This is shown by the experimental results plotted in Fig. 3g, where we compare the time-averaged power spectra for the “AB” and “BA” sequences. These spectra are computed by integrating the temporal data in Fig. 3e. When only signal “A” or only signal “B” is applied, we measure conventional spontaneous three-magnon splitting of the respective primary modes with the secondary modes already discussed above in the context of Fig. 3b. Within the overlap interval, the mutual cross-stimulation leads to additional peaks in the scattered mode spectrum. As highlighted by shaded areas in Fig. 3e, the frequencies and amplitudes of these additional scattered modes strongly depend on the temporal order of the two input signals. Consequently, the average spectra of “AB” and “BA” are different from each other, and neither can be constructed from a simple superposition of the average spectra of “A” and “B” individually (Fig. 3g). This is the key principle that underpins how the magnon-scattering reservoir processes temporal signals.

To highlight the significance of the transient times, we vary the overlap Δt of the symbols “A” and “B” in experiments and determine the frequency-averaged difference between the time-averaged spectra of “AB” and “BA” (Fig. 3h). This difference is zero when the two input pulses do not overlap since no cross-stimulation takes place. With increasing overlap, however, cross-stimulation between the two pulses becomes more significant and leads to a difference in the output of the reservoir. This difference vanishes again when the input pulses fully overlap and, thus, arrive at the same time.

To explore the capabilities of the presented MSR, the complexity of the input signals was further increased experimentally. Figure 4a shows the nonlinear response to the four-symbol pulse pattern “ABAB” measured by TR-µBLS. In contrast to a reference spectrum composed of a simple linear superposition of two consecutive “AB” patterns, shown in Fig. 4b, the real spectrum of the four-symbol response contains additional features that are generated by cross-stimulated scattering when two pulses overlap. The differences are highlighted by the shaded areas in Fig. 4a and circled areas in Fig. 4b, respectively. This behaviour illustrates that cross-stimulation can result in distinct features that allow distinguishing longer patterns. This is further exemplified in Fig. 4c, which shows the time-averaged BLS spectra of the six four-symbol combinations comprising two “A” and two “B”. Like the data in Fig. 3, transient processes from cross-stimulation generate distinct power spectra for the six combinations, which would be indistinguishable in the linear response regime.

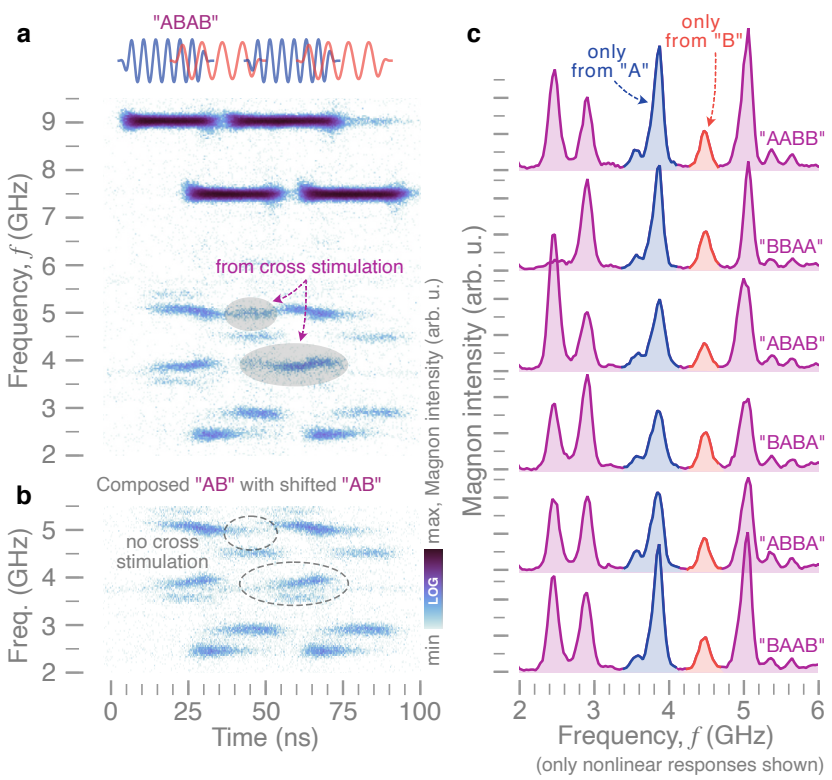

Fig. 4: Performance of the magnon-scattering reservoir (MSR) for longer temporal patterns characterized experimentally. (a) Time-resolved spectral response of the MSR to a four-symbol microwave pattern "ABAB", detected experimentally with TR-μBLS. (b) For reference, the spectrum of "AB" is overlayed with a shifted version of itself. Differences between composed and real spectrum (due to cross-stimulated magnon scattering) are highlighted by shaded and circled areas. (c) Average output spectra of the MSR for different four-symbol patterns with the same average input-frequency content but clearly different nonlinear responses. Taken from [L. Körber et al., *Nature Comm.* 14, 3954 (2023)].

Since the experimental data discussed so far requires the integration of thousands of pulse cycles, we rely on micromagnetic simulations to quantify the capacity of the magnon-scattering reservoir for recognizing all possible combinations of four-symbol sequences composed from "A" and "B". Thereby, we can analyze individual pulse sequences and study the influence of thermal noise and amplitude fluctuations on the recognition rate of the MSR. Figure 5a shows a simulated power spectrum (at temperature T = 300 K) for the input pattern "ABAB" with f_A = 8.9 GHz ($b_{rf,A}$ = 3 mT) and f_B = 7.4 GHz ($b_{rf,B}$ = 3.5 mT), with the field strengths chosen to be above the respective power threshold for three-magnon splitting. The output spaces of the reservoir are defined by subdividing the time-averaged power spectrum into frequency bins of different widths. To emphasise the importance of the scattering (interconnection) between the different magnon modes, we study the performance of the magnon-scattering reservoir for two separate output spaces (Fig. 5a). One output space for the scattered modes is constructed over a 4-GHz window below f_A and f_B, where the different frequency bins result in an output vector with 16 to 80 components depending on the bin size. For comparison, a two-dimensional output space corresponding to the directly excited modes is constructed by averaging within bins centred around f_A and f_B. Note that, analyzing the directly excited modes does not correspond to a linear classifier, as these modes themselves experience nonlinear feedback (amplitude losses, frequency shift, etc.) above their power threshold for three-magnon splitting.

For each four-symbol sequence, 200 micro-magnetic simulations were executed with different realizations of the thermal field to generate distinct output states. Supervised learning using logistic regression was then performed on this data set to construct trained models of the output states based on either the directly excited or scattered modes. The accuracy of these models for different combinations of input frequencies f_A = 8.9GHz, f_B = 7.2GHz, f_C = 6.5GHz, f_D = 10.7 GHz (and corre-

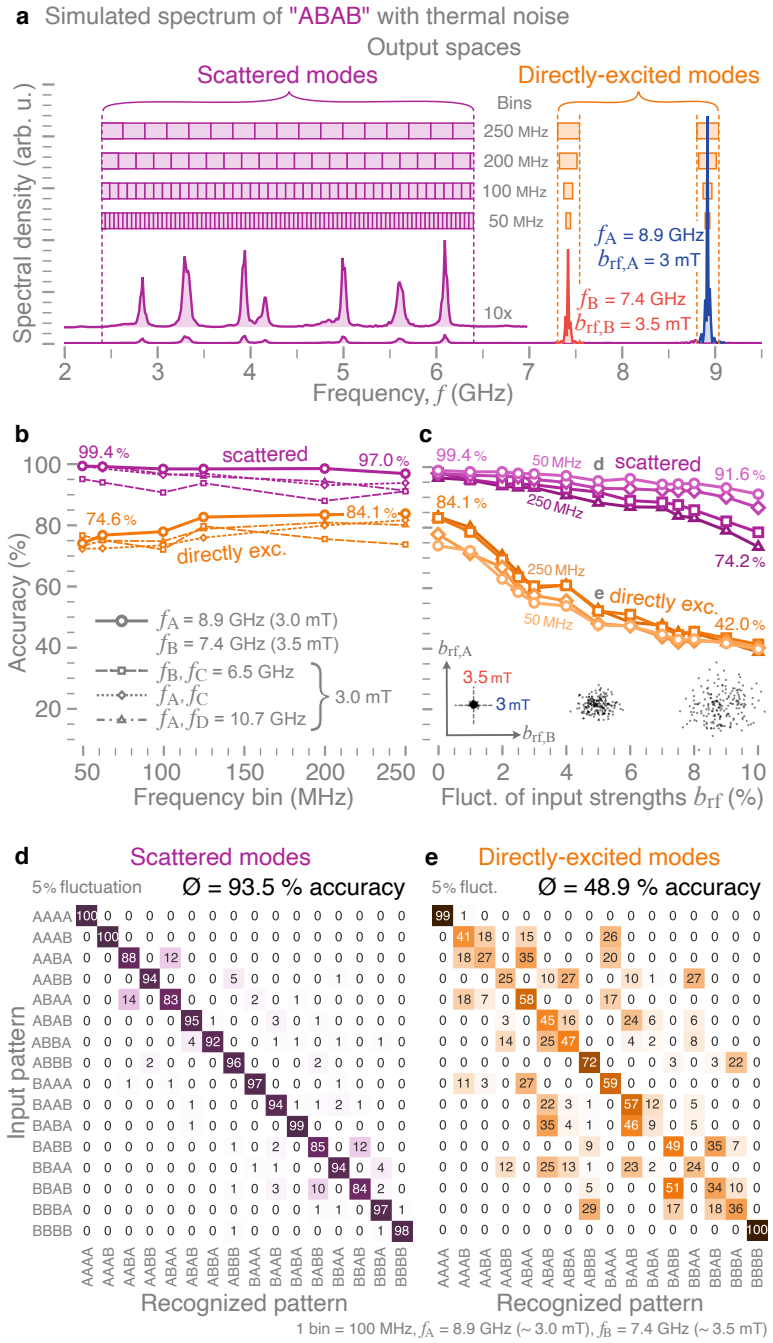

Fig. 5: Micromagnetic modeling of pattern recognition capabilities. (a) Simulated spectrum of the pattern "ABAB" with the definition of different output spaces (scattered and directly excited modes) for the magnon-scattering reservoir. (b) Average detection accuracy of four-symbol patterns for different output spaces and excitation frequency and power combinations as a function of frequency bin sizes. (c) Accuracy for different output spaces and bin sizes as a function of power fluctuations in the input signals (depicted by the insets). (d), (e) Corresponding confusion matrices for the two output spaces, respectively, both for the same frequency combination, bin size, and input power fluctuation. Taken from [L. Körber et al., *Nature Comm.* 14, 3954 (2023)].

sponding input strengths $b_{rf,i}$) is shown in Fig. 5b as a function of bin size. We find that the magnon-scattering reservoir performs comparably well when choosing different input frequencies (different radial modes) to represent the input symbols. Hence, an extension of the input space to more than two frequencies/symbols ("ABC", "BDC", "ABCD", etc.), or even to more broadband signals, is straightforward. This is corroborated by the experimental data plotted in Fig. 6.

Overall, the accuracy depends weakly on the bin size. The recognition rate slightly increases with increasing bin size for the directly-exited modes whereas it decreases marginally for the scattered modes. This can be understood from the fact that smaller bin sizes capture more features of the power spectrum of the scattered modes, while for the directly-excited modes, the larger bin sizes contain more information about potential nonlinear frequency shifts, which helps to separate the inputs. We observe that outputs based on the directly-excited modes can yield an accuracy of

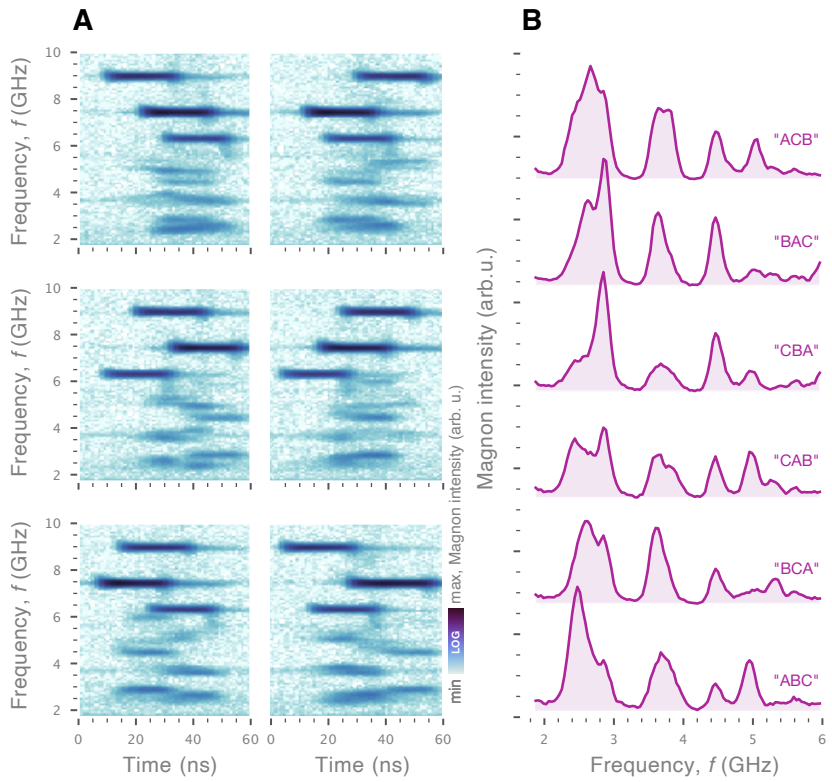

Fig. 6: (a) Time-resolved spectral response of the magnon-scattering reservoir to a three-symbol microwave pattern "ABC", detected with TR-μBLS, where f_A = 8.9 GHz (25 dBm), f_B = 7.4 GHz (23 dBm), f_C = 6.3 GHz (20 dBm). The input consists of 3 pulses, each with a duration of 20 ns and an overlap of 10 ns. (b) Time averaged spectra of the magnon-scattering reservoir in response to different permutations of the three input frequencies. Taken from [L. Körber et al., *Nature Comm.* 14, 3954 (2023)].

~84%, while scattered modes provide a notable improvement in performance, with an accuracy reaching 99.4% for the case considered in Fig. 5a. In general, the scattered modes provide higher accuracy for pattern recognition compared with the directly-excited modes. The difference in accuracy becomes even more pronounced when amplitude fluctuations are present. Figure 5c illustrates how the accuracy evolves with the fluctuation strength, which represents the width of the normal distributions (in %), centred around the nominal values of $b_{rf,A}$ and $b_{rf,B}$, from which the field strengths are drawn, as shown in the inset for $b_{rf,A}$ = 3 mT and $b_{rf,B}$ = 3.5 mT. The performance of the magnon-scattering reservoir based on the directly excited modes drops significantly with increasing fluctuation strength to 42% accuracy at 10% fluctuation. However, recognition based on the scattered modes is much more resilient, with a decrease to only between ~74% and ~92% accuracy (depending on the bin size).

Figures 5e,f show confusion matrices for the scattered and directly excited modes, respectively, both for the same set of parameters. They highlight the robustness of the magnon-scattering reservoir which is based on the scattered modes since it mainly fails to distinguish "AABA" from "ABAA" and "BBAB" from "BBAB" in ~12% of the cases. The magnon-scattering reservoir based on the directly excited modes, on the other hand, fails to recognize almost all of the patterns, except for the trivial cases of "AAAA" and "BBBB" for which there is practically no ambiguity in the inputs. These trends do not depend on the type of supervised learning used and highlight the important role of cross-stimulated three-magnon splitting in the magnon reservoir for the pattern recognition of noisy radiofrequency signals.

Our findings demonstrate the possibility of performing reservoir computing in modal space utilizing the intrinsic nonlinear properties of a magnetic system, namely the scattering processes between magnons in a magnetic vortex disk. Temporal patterns encoded using two different input-frequency pulses can be distinguished with high accuracy. The results also indicate that input patterns can be extended to more broadband signals. It is important to mention that the technical design of the

physical reservoir is simple and requires very little prepossessing, while the complexity of the data handling arises mostly from the intrinsic nonlinear dynamics of the magnon system. Additionally, as we will discuss in Section 4, magnon interactions in micrometre-sized disks can be modified significantly by small static magnetic fields, providing an effective means to enhance the complexity of the vortex-based magnon reservoir further.

3. Short-term memory and parity check

The short-term memory (STM) and parity check (PC) tasks are popular metrics to evaluate the performance of a physical reservoir.[26] While the STM task yields a measure of the fading memory of the reservoir, the PC task provides the reservoir's ability to perform nonlinear computations. Therefore, we have carried out both tasks in the experiment and the simulation. In both cases, we have used a binary sequence of 1000 pulses with a random distribution of "A" and "B" as input $u(T)$ to the reservoir and acquired the power spectral density of the scattered modes. As already discussed in the previous section, "A" and "B" are represented by radiofrequency (rf) signals, which consist of 14-ns long sine wave pulses with two distinct frequencies, f_A = 7.4 GHz (24 dBm) and f_B = 8.9 GHz (20 dBm). The excitation amplitudes given in brackets were chosen to be above the threshold for three-magnon scattering.

The output state of the reservoir, $x(T)$, represents the power spectral density averaged throughout the pulse at the time T. The STM task involves predicting inputs from the past based on the present state of the reservoir, where we can define the target output $\hat{y}_{out}(T,\tau)$ as the input with a time delay τ

$$\hat{y}_{out}(T,\tau) = u(T-\tau). \qquad \text{(STM)}$$

Training involves constructing the matrix $\mathbf{W}$ such that

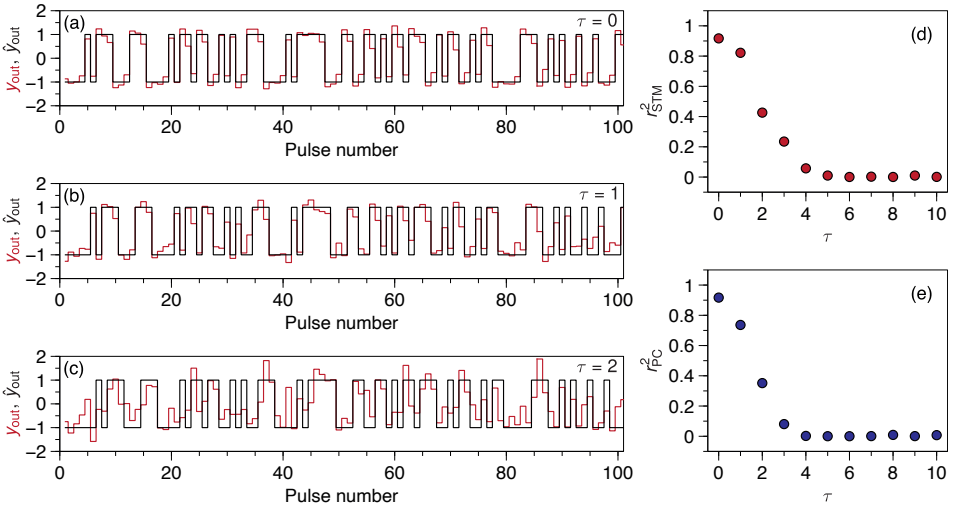

Fig. 7: Short-term memory (STM) and parity check (PC) tests of the experimental magnon-scattering reservoir. (a)-(c) Comparison between the target $\hat{y}_{out}$ and trained y_{out} outputs for three delays τ for the STM task. (d),(e) Square of the correlation coefficient for (d) the STM and (e) the PC tasks.

[26] Furuta, T. et al. Macromagnetic Simulation for Reservoir Computing Utilizing Spin Dynamics in Magnetic Tunnel Junctions. *Physical Review Applied*, 10, 034063 (2018).

$$\mathbf{W}x(T) = y_{out}(T) \approx \hat{y}_{out}(T).$$

Here, we have used 800 pulses for training and 200 pulses for testing. In Fig. 7a-c, we show the target $\hat{y}_{out}$ and output y_{out} values of the STM task for the experimental reservoir for three values of the delay τ. We can see that reconstruction of the output signal works reasonably well for the first few values of the delay, which indicates that there is short-term memory in the system. This can be quantified with the square of the correlation coefficient,

$$r_{STM}(\tau)^2 = \frac{cov\left(y_{out}, \hat{y}_{out}\right)^2}{cov\left(y_{out}, y_{out}\right) \times cov\left(\hat{y}_{out}, \hat{y}_{out}\right)}$$

where $cov(a, b)$ is the covariance between two vectors a and b. $r_{STM}(\tau)^2$ takes values between 0 and 1, with one demonstrating the exact prediction of the target output, and zero showing no correlation between the actual output and the target output. $r_{STM}(\tau)^2$ is shown as a function of delay for the STM task in Fig. 7d.

With the same data, we also performed the same analysis for the PC task,

$$y_{PC}(T, \tau) = u(T) \oplus u(T-1) \oplus \ldots \oplus u(T-\tau) \qquad \text{(PC)}$$

where $\oplus$ designates the XOR function. The square of the correlation coefficient for the PC task $r_{PC}(\tau)^2$ is plotted in Fig. 7e. As these results show, the magnon scattering reservoir exhibits short-term memory and is capable of performing nonlinear tasks like XOR.

Fig. 8 shows the same analysis performed for the simulated magnon reservoir, where we can observe similar metrics for the STM and PC tasks.

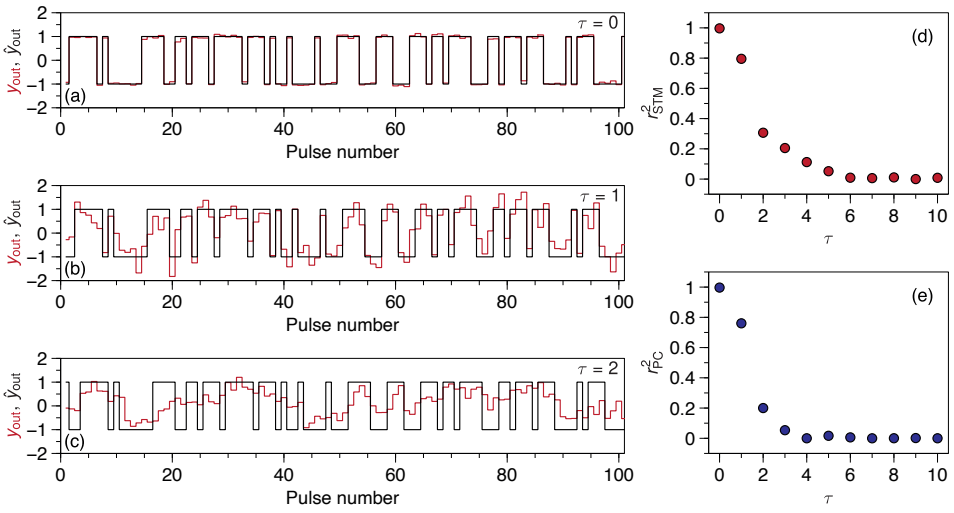

Fig. 8: Short-term memory (STM) and parity check (PC) tests of the simulated magnon-scattering reservoir. (a)-(c) Comparison between the target $\hat{y}_{out}$ and trained y_{out} outputs for three delays τ for the STM task. (d),(e) Square of the correlation coefficient for (d) the STM and (e) the PC tasks.

4. Modification of three-magnon splitting in a flexed magnetic vortex

So far, we discussed three-magnon splitting in confined vortices in the absence of external fields, where the vortex core is centred within the magnetic disk. As a next step, we study the influence of an in-plane magnetic field on the nonlinear magnon dynamics and, hence, the vortex-based

magnonic reservoir. The application of an in-plane magnetic field leads to the displacement of the vortex core from its centre position and to a flexing of the vortex skirt. Our study is carried out numerically using micromagnetic simulations and experimentally using Kerr microscopy and micro-focused Brillouin-light-scattering (μBLS) spectroscopy. The results of this work have been published in Applied Physics Letters[27]. A preprint is available on the arXiv server[28].

For our study, we consider the same magnetic disk as already discussed before, which consists of 50-nm thick Ni_{81} Fe_{19} (permalloy, Py) with a diameter of 5.1 μm, as seen in Fig. 9a. The presence of the vortex state at zero field is confirmed with micromagnetic simulations and Kerr microscopy. In Fig. 9a, we present the in-plane angle of the magnetization obtained with both methods as a colour map superimposed on the top surface of the magnetic disk.

To discuss the deformation of the vortex under the application of an in-plane external magnetic field B (here, applied in y direction), it is useful to consider the contour lines of the magnetization component m_x = const. perpendicular to the magnetic field. In the following, we only show the contour lines (as dotted lines) obtained from the numerical data. At zero field, these contours are straight lines, in agreement with an absence of magnetic volume charges $\rho = -M_S \nabla m$. With increasing vortex displacement, these charges become nonzero and play an important role in the magnon dynamics. In the field-free case, the magnon modes can be characterized by their number of nodal lines n = 0, 1, 2, … in the radial direction and their number of periods m = 0, ±1, ±2 in the

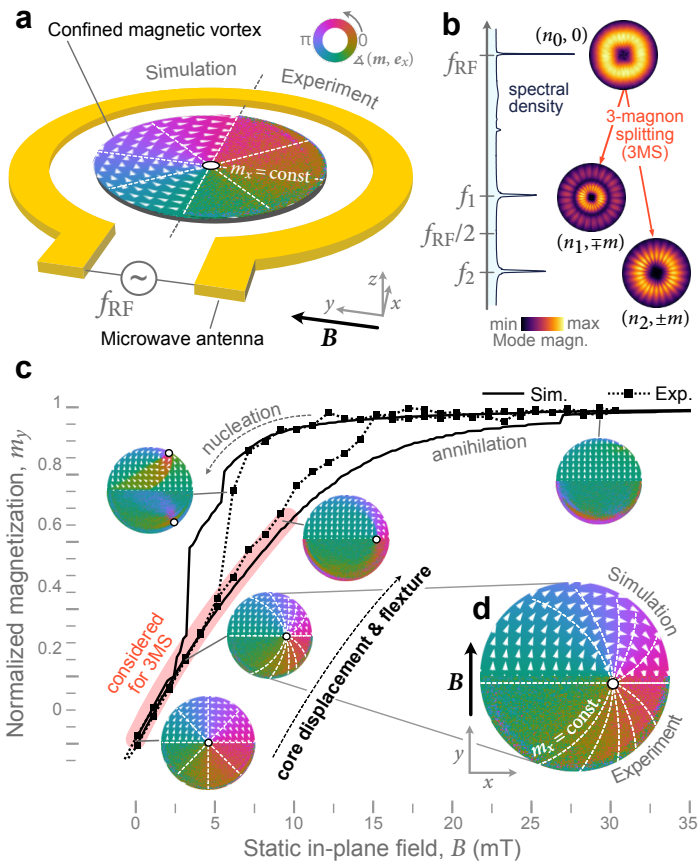

Fig. 9: (a) Schematics of a Py disk and of the antenna design used in the experiments. At remanence, the disk exhibits a vortex state, confirmed with micromagnetic simulations and, experimentally, with Kerr microscopy. The colour code depicts the in-plane angle of the magnetization, obtained with both methods. A white circle indicates the position of the vortex core where the magnetization tilts out-of-plane. Dashed lines denote the contour lines of constant m_x obtained from the simulations. (b) Exciting a radial mode above the threshold triggers nonlinear three-magnon splitting, and pairs of modes with frequencies $f_{1,2} = f_{RF} \pm \Delta f$ and different radial profiles are excited. The shown spatial mode profiles have been obtained from micromagnetic simulations. (c) Measured (dotted line) and simulated (solid line) hysteresis loop segment of the vortex disk with in-plane external field is shown. The magnetization distribution for certain field values is added as insets, in which the colour code represents the experimentally and numerically obtained in-plane angle of the magnetization states. Taken from [L. Körber arXiv:2211.08226 (2023)].

[27] Körber, L. et al. Modification of three-magnon splitting in a flexed magnetic vortex. *Appl. Phys. Lett.* 122, 092401 (2023).

[28] Körber, L. et al. Modification of three-magnon splitting in a flexed magnetic vortex. arXiv:2211.08226 (2023).

azimuthal direction. An Ω-shaped microwave antenna is used to excite radial magnon modes with $m = 0$ at frequency f_{RF}. When the input power is high enough, three-magnon splitting sets in, i.e., the primary radial mode splits into two secondary modes with opposite azimuthal indices $\pm m$ (conservation of angular momentum), distributed around half the excitation frequency $f_{1,2} = f_{RF} \pm \Delta f$ (conservation of energy), as seen in Fig. 9b. An additional selection rule requires the two secondary modes to exhibit different radial indices, resulting in a frequency split $\Delta f \neq 0$ between them.

Before we explore the influence of vortex deformation on three-magnon splitting, we study the effect of an externally applied magnetic field on the vortex state itself, in particular, its in-plane hysteresis loop. For this, we sweep the external field from 0 to 40 mT (and back), tracking the vortex state with micromagnetic simulations and Kerr microscopy. In Fig. 9c, we show the evolution of the magnetization component m_y parallel to the applied field together with two-dimensional maps of the vortex state at certain points of the loop. For moderate in-plane fields (below 15 mT), the vortex core is displaced from its centre position which leads to a growth of the region of the vortex skirt magnetized parallel to the field (green area in the angle maps). However, in parallel to this displacement of the core, the skirt of the vortex is not simply displaced transversally to the field (which would correspond to a rigid-vortex model). Instead, the vortex skirt flexes to keep the magnetization parallel to the sides of the disk which avoids magnetic edge charges and, thus, minimizes stray fields. This can be seen nicely in Fig. 9d, as the contour lines of m_x bend (deviating from rigid core displacement).

Finally, after further increasing the applied magnetic field, the vortex core reaches the boundary of the disk and annihilates, allowing for a saturation of the magnetic sample. When decreasing the external field from saturation, two vortices nucleate at the boundary, which move together and finally merge to a single vortex close to zero applied field. We highlight that, in Fig. 9c, this two-vortex nucleation is seen in both experiment and simulation, attesting to the good agreement between both methods.

For the following study of nonlinear magnon interaction, we shall restrict ourselves to the field range from 0 → 10 mT in which the vortex core is merely displaced, as marked in Fig. 9c. We start again at zero field and excite the confined vortex with an out-of-plane microwave field at $f_{RF} = 6.1$ GHz. In the micromagnetic simulations, the strength of the field is set to $b_{RF} = 2.8$ mT. In our experiments, we set the microwave output power to $L_P = 17$ dBm. Even though it is experimentally cumbersome to determine the exact microwave power arriving at the sample and, thus, compare it with the field applied in the simulations, in both cases, the radial mode ($n = 0, m = 0$) is excited above its threshold for three-magnon splitting. In experiments, the spectral response of the system is probed using μBLS and in simulations, using Fourier analysis. As seen in Fig. 10a, nonlinear splitting of the excited primary mode leads to two secondary modes around half the excitation frequency. Additional frequency contributions can be attributed to higher-order processes (e.g. four-magnon-scattering between the secondary modes) and will not be considered in the following discussion.

To investigate the field dependence of the spectral response, we increase the external field to displace the vortex core from its centre position while maintaining the microwave excitation fixed at 6.1 GHz. The corresponding spectral response as a function of the applied field is shown as colour maps in Fig. 10a (simulation) and Fig. 10b (experiment). For very small fields (≲ 2.5 mT) we see that the frequency split Δf between the secondary modes decreases slightly. As a first observation,

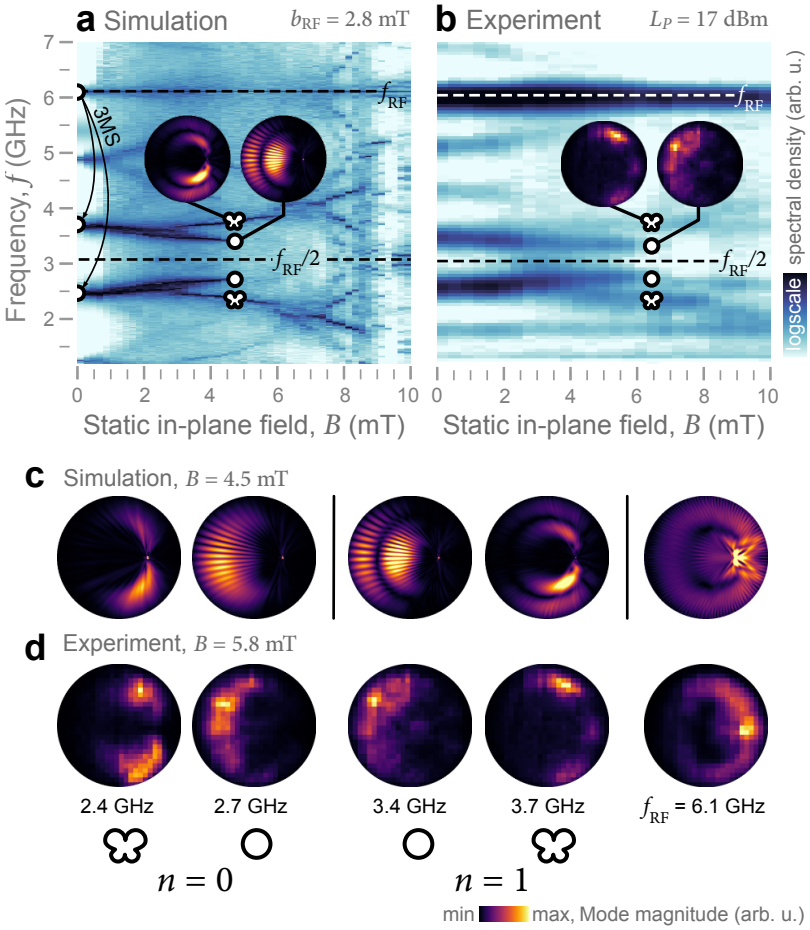

Fig. 10: (a) Numerically and (b) experimentally obtained frequency response of the magnetic vortex excited at f_{RF} = 6,1 GHz above the threshold for three-magnon splitting as a function of the applied in-plane magnetic field. At zero field, only one pair of secondary modes is created around $f_{RF}/2$ by three-magnon splitting. With increasing inplane magnetic field, the vortex is deformed which leads to a splitting of the three-magnon response into several branches, corresponding to the regular vortex modes and additional butterfly modes, as seen in the mode profiles. (c) Numerical and (d) experimental profiles of all modes at a given vortex-displacement (in-plane field), showing that regular and butterfly modes are arranged in pairs which satisfy the selection rules of three-magnon splitting in vortices. Taken from [L. Körber arXiv:2211.08226 (2023)].

overall, three-magnon splitting is found to be robust against vortex deformation. However, with increasing in-plane field (see Figs. 10a,b), we observe a splitting of the secondary modes into several branches. This splitting continues for even higher in-plane fields. To identify the different branches, we obtain the spatial modes profiles at $B = 4.5$ mT in the simulations using inverse Fourier transform at the respective frequencies. In our experiments, the spatial mode profiles are obtained at $B = 5.8$ mT by scanning the whole sample with BLS microscopy. These two external fields were chosen to achieve well-separated peaks in the frequency spectra obtained with each method. Their difference can again be justified by the uncertainty in microwave power and external field mentioned above, as well as by the lower spectral resolution in the experiments. The numerical mode magnitude corresponds to the local magnitude $|m_z(\mathbf{r}, f)|$ of the corresponding Fourier component of the dynamic magnetization, which is proportional to the photon counts we measure in our BLS experiments.

The profiles of all modes (directly excited and secondary) are shown for both methods in Figs. 10c,d. We find that the different branches correspond to two qualitatively distinct classes of modes. The first class of modes resembles the regular modes of a magnetic vortex and are merely deformed versions of the modes in a centred vortex. For the chosen magnetic field, these modes oscillate at 2.7 GHz and 3.4 GHz. The second class of modes is characterized by unconventional spatial profiles, resembling the shape of a butterfly with the vortex core at its centre (2.4 GHz and 3.7 GHz). These modes are arranged in separate pairs, a pair of regular secondary modes and a pair of butterfly secondary modes. Each of these pairs satisfies the three-magnon resonance condition $f_{1,2} = f_{RF}/2 \pm \Delta f$. It is quite remarkable that, even though the cylindrical symmetry of the system

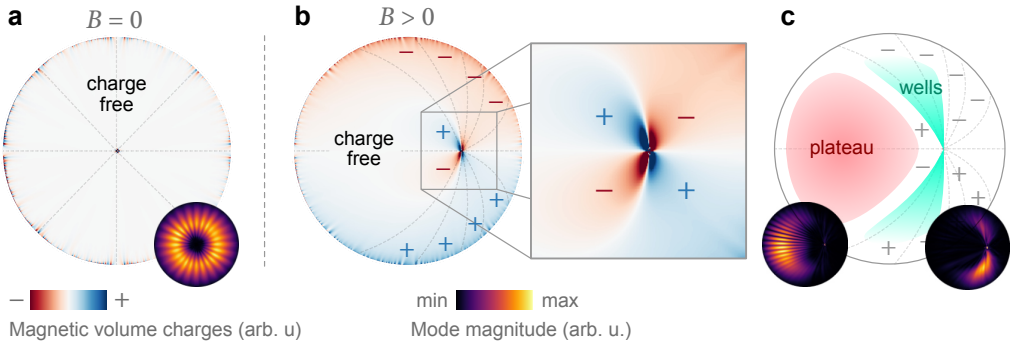

Fig. 11: Static magnetic-volume charges in a (a) centered vortex at zero in-plane field and a (b) flexed vortex at non-zero in-plane field. Whereas at zero field, only one class of modes is present, at finite field, the flexing of the vortex skirt leads to (c) plateaus and wells in the internal dipolar energy of the vortex, leading to two different classes of modes (regular on the plateau and butterfly shaped in the wells). Taken from [L. Körber arXiv:2211.08226 (2023)].

is broken and the characterisation of the modes in terms of radial and azimuthal mode numbers becomes ambiguous, the secondary modes within one scattering channel (regular or butterfly) still obey certain selection rules which lead to a non-zero frequency split between them. In the numerically obtained mode profiles in Fig. 10c, it can be seen how the modes in each pair still have a different number of nodal lines along the new "radial" direction. This retaining asymmetry between the spatial profiles of the secondary modes is not surprising, as the vortex still inherits a mirror symmetry even when deformed into a flexed state. Such mirror symmetry alone can lead to selection rules for three-magnon splitting, as is the case in magnetic films.[29]

The splitting of the spectrum of secondary modes into two classes can be understood in a simple picture by considering the landscape of magnetic volume charges created by deforming the magnetic vortex. To illustrate this, in Fig. 11, we show the volume charges for a centred and a deformed vortex observed from our simulations. At zero field (Fig. 11a), the vortex achieves to suppress volume charges almost everywhere by forming a perfectly azimuthal rotation of in-plane magnetization, except close to the vortex core. As a result, the spectrum is only comprised of the well-known regular vortex modes described by azimuthal and radial mode numbers. For finite static in-plane fields, the flexing of the vortex skirt leads to an accumulation of magnetic volume charges adjacent to the core and at the boundaries of the magnetic disk close to the core, as seen in Fig. 11b. As shown in Fig. 11c, this charge distribution leads to potential wells for a bound magnon state similar to the channelled magnons in Néel-type domain walls.[30] These bound modes have already been observed with a low number of periods around the vortex core in Refs. [31,32]. In said works, the authors used linear excitation with in-plane microwave fields or direct spin-polarized currents to excite these modes. Both works, however, did not experimentally verify the spatial character of these modes. Apart from the flexed part of the vortex skirt, an (almost) charge-free region remains at the opposite side of the disk, leading to a potential plateau for the regular "free" vortex modes.

In the following, we will see that the observed bound/butterfly modes exhibit a much lower power threshold for three-magnon splitting than the regular modes in a centred vortex. Again, we sweep the static in-plane field from 0 to 10 mT, however, this time, for different magnitudes/powers of the

[29] L'vov, V. S. Wave Turbulence Under Parametric Excitation: Applications to Magnets (Springer, Berlin, Heidelberg, 1994).

[30] Wagner, K. et al. Magnetic domain walls as reconfigurable spin-wave nanochannels. *Nat. Nanotechnol*. 11, 432–436 (2016).

[31] Aliev, F. G. et al. Spin waves in circular soft magnetic dots at the crossover between vortex and single domain state. *Phys. Rev. B* 79, 174433 (2009).

[32] Jenkins, A. S. et al. Electrical characterisation of higher order spin wave modes in vortex-based magnetic tunnel junctions. *Commun. Phys.* 4, 107 (2021).

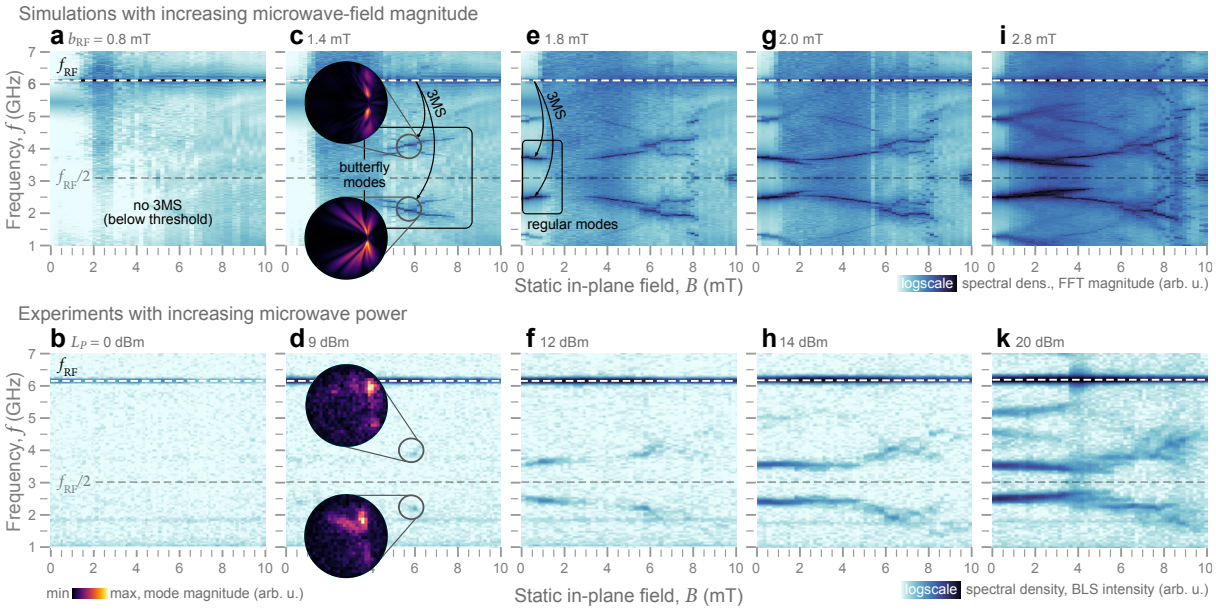

Fig. 12: Evolution of the numerically and experimentally obtained frequency response of the magnetic vortex excited at a fixed microwave-excitation frequency of 6.1 GHz with increasing magnitudes/powers of the driving microwave source for in-plane fields between 0 and 10 mT. For low excitation (a) and (b), only the primary magnon mode can be seen. At slightly higher excitations, panels (c) and (d) secondary modes appear for static fields for which the vortex is strongly distorted. The mode profiles obtained both from simulations and experiments are shown as insets and demonstrate that these modes are butterfly shaped modes localized to the highly flexed regions of the vortex skirt. Further increasing the excitation strength, shown in (e) and (f), leads to the appearance of the 3MS for regular vortex modes close the zero in-plane field, confirming that the three-magnon splitting into butterfly modes has a lower threshold power. Finally, at large excitation strengths, a rich and complex frequency response is measured, summarized in panels (i)–(k). Taken from [L. Körber arXiv:2211.08226 (2023)].

driving microwave field. We start with a microwave power below the nonlinear three-magnon splitting threshold, at $b_{RF} = 0.8$ mT. We see in Fig. 12a,b (simulation and experiment, respectively) that only the primary magnon at $f_{RF} = 6.1$ GHz is excited over the whole field range and no additional secondary modes. With increasing microwave power (Fig. 12c,d), secondary modes appear for static fields ≳ 4.5 mT at which the vortex is deformed considerably. Analyzing the spatial mode profiles of these modes from experiments and simulation reveals that all of them are indeed modes localized to the highly flexed regions of the vortex skirt (shown as insets in Fig. 12c,d). Note again, that all of them are arranged in pairs with frequencies $f_{1,2} = f_{RF}/2 \pm \Delta f$ and different "radial" profiles. Only when increasing the microwave power even further, the three-magnon splitting threshold of the regular vortex modes is reached (Fig. 12e,f), and their frequency contribution is visible at small in-plane fields at which the vortex is hardly deformed. Finally, with further increasing the microwave power, the branches of the two pairs of modes approach each other until they overlap in the in-plane-field range, and ultimately, the behaviour discussed in the context of Fig. 10 is recovered.

The reason the butterfly modes inherit a lower threshold for three-magnon splitting compared to the regular vortex modes can be two-fold: First, their intrinsic damping rates $\Gamma_{1,2}$ could be significantly lower which would point towards lower mode ellipticities, or, second, their three-magnon scattering coefficients $V_{0,12}$ concerning the directly-excited (primary) magnon are significantly larg-

er.[33] A combination of both factors finally results in lower thresholds for the driving microwave fields $b_{RF,crit} \propto \Gamma_1\Gamma_2/|V_{0,12}|$.

With our study of three-magnon splitting in a flexed magnetic vortex, confined to a micrometre-sized magnetic disk, we have shown that this nonlinear process is stable concerning the displacement of the vortex core by in-plane magnetic bias fields. Application of such fields leads to a flexing of the vortex skirt, which, in return, leads to a separation of the secondary modes produced by three-magnon splitting into modes corresponding to the regular radial and azimuthal modes of a symmetric vortex, and, into additional butterfly modes which are confined to the highly flexed regions adjacent to the vortex core. Splitting into these additional secondary modes exhibits a much lower power threshold than into the regular vortex modes. With this work, we expand the understanding of three-magnon splitting in confined magnetic systems, providing a way to excite unconventional magnon modes in flexed magnetic vortices. Furthermore, small in-plane bias fields, in the range of a few tens of mT are shown to be a powerful parameter to tune the characteristics of microscopic nonlinear systems in place, which makes them an efficient tool to tune our vortex-based magnon reservoir.

[33] Verba, R. et al. Theory of three-magnon interaction in a vortex-state magnetic nanodot. *Phys. Rev. B* 103, 014413 (2021).